Research Square

Preprints are preliminary reports that have not undergone peer review.
They should not be considered conclusive, used to inform clinical practice,
or referenced by the media as validated information.

Multimodal CT Radiomics–Dosiomics Fusion Predicts Local Recurrence and Survival after Low-Dose-Rate Brachytherapy for Salivary Gland Carcinoma

Zhenyu Li
Peking University School and Hospital of Stomatology
Guohao Zhang
Peking University School and Hospital of Stomatology
Xiaoying Wang
Peking University School and Hospital of Stomatology
Zhuo Xiao
Beihang University
Yiwei Zhong
Sun Yat-sen University
Bo Liu
Beihang University
Mingwei Huang
hmwd97@126.com
Peking University School and Hospital of Stomatology

Research Article

Keywords:

Posted Date: March 24th, 2026

DOI: https://doi.org/10.21203/rs.3.rs-8156737/v1

License: This work is licensed under a Creative Commons Attribution 4.0 International License. Read Full License

Additional Declarations: No competing interests reported.

Abstract

Background

Salivary-gland carcinomas (SGCs) are histologically diverse with variable prognoses. For postoperative residual disease treated by ^{125}I low-dose-rate (LDR) brachytherapy, conventional prognostic factors are insufficient for individualized risk stratification. Radiomics and dosiomics quantify tumor phenotype and three-dimensional dose heterogeneity and may offer complementary prognostic value.

Methods

We retrospectively analysed 263 SGC patients treated with ^{125}I LDR brachytherapy (2011–2019). Radiomic features (planning CT) and dosiomic features (post-implant 3D dose maps) were extracted with PyRadiomics and filtered for redundancy. Five Cox models (clinical, DVH, radiomics, dosiomics, hybrid) were trained with 30% held-out internal validation. Temporal external validation was performed in an independent 2020 cohort (n = 74; all survivors ≥ 5-year follow-up). Performance was assessed by Harrell's C-index, time-dependent AUCs at 1/3/5 years, integrated Brier score (IBS), decision-curve analysis (DCA), and KM risk stratification.

Results

For local recurrence (LR), the radiomics model was the best single-modality model internally (C-index 0.86), while the hybrid model performed best overall (C-index 0.87). For overall survival (OS), a parsimonious four-variable hybrid achieved the highest internal discrimination (C-index 0.63). In the external 2020 cohort, the hybrid model maintained out-of-sample performance: LR—C = 0.714; AUCs 0.645/0.722/0.732; IBS 0.090; OS—C = 0.859; AUCs 0.945/0.887/0.909; IBS 0.030, with positive net benefit on DCA and clear KM separation.

Conclusions

Radiomics captures intratumoral heterogeneity relevant to local control, while dosiomics contributes independent dose-heterogeneity information for survival. Integrating both with clinical variables yields the most accurate LR prediction and improves OS discrimination.

Introduction

Salivary gland carcinomas (SGCs) are rare and heterogeneous malignancies within the spectrum of head and neck cancers, accounting for approximately 3% to 8.5% of all head and neck cancer diagnoses[1]. Salivary glands are divided into three pairs of major glands—the parotid, submandibular and sublingual glands—and minor glands scattered throughout the mucosa of the oral cavity, oropharynx and upper aerodigestive tract. The prognosis of SGC varies widely depending on tumor stage, histologic subtype, and treatment modality. Early-stage or low-grade tumors often achieve good control with surgery and adjuvant radiotherapy, whereas advanced or high-grade SGCs carry higher risks of recurrence and metastasis. In cases where surgery is not feasible or as an adjunct to surgery, interstitial brachytherapy has been employed as a means of delivering high radiation dose to the tumor with rapid dose fall-off sparing adjacent normal tissues[2]. Low-dose-rate (LDR) brachytherapy using permanent implanted seeds can provide effective local control in inoperable salivary gland tumors while minimizing exposure to surrounding structures[3]. Conventional prognostic factors, including tumor size, patient age, and the number of positive lymph nodes, have been commonly utilized for risk stratification in parotid gland carcinoma patients undergoing adjuvant radiotherapy[4], but they do not fully capture the complexity of individual tumors. There is a critical need for more precise predictive tools to identify which patients are at higher risk of treatment failure, in order to personalize therapy.

In recent years, radiomics has emerged as a promising approach to extract quantitative biomarkers from medical images. Radiomics involves the high-throughput extraction of a large number of features from radiographic images, capturing characteristics of tumor intensity, shape, and texture that are not discernible by human inspection[5]. For example, a multicenter study demonstrated that an integrated radiomics-clinical model derived from pretreatment CT scans could predict overall survival in non-small cell lung cancer patients treated with immunotherapy more accurately than clinical parameters alone[6]. In salivary gland malignancies, a recent study incorporating PET/CT radiomic features achieved a concordance index (C-index) of 0.83 for overall survival – significantly higher than models based on stage alone (C-index ~ 0.65)[7].

While most radiomics research has focused on diagnostic or pre-treatment imaging, interest is growing in applying similar analyses to radiation dose distributions, an approach known as dosiomics[8]. Recent studies support this: Murakami et al. developed a dosiomics model for prostate-cancer intensity-modulated radiation therapy (IMRT) and showed that spatial dose-texture descriptors extracted from the clinical target volume predicted biochemical recurrence more accurately than conventional DVH metrics[9]. Similarly, Zhang et al. introduced an integrative radiomics and dosiomics model for lung cancer patients and found that spatial features of the lung dose distribution predicted radiation pneumonitis risk more accurately than mean lung dose alone[10].

To date, few studies have systematically evaluated radiomic and dosiomic predictors in the brachytherapy setting for any tumour site, and none has focused on salivary-gland carcinoma—a disease in which the spatially discrete radioactive sources yield highly heterogeneous dose distributions. Consequently, the influence of intra-target cold and hot spots on tumour control or toxicity in this patient population remains largely undefined. We hypothesize that by extracting quantitative features from both imaging and dose data, we can improve the accuracy of predicting treatment outcomes for these patients. In this retrospective study, we integrated radiomic features from pre-implant CT images, dosiomic features from post-implant dose distributions, clinical factors, and DVH metrics into predictive models. The goal was to identify which features are most strongly associated with outcomes in SGC patients treated with low-dose-rate interstitial brachytherapy.

Materials and Methods

Patients

A total of 263 patients with malignant salivary-gland carcinoma were retrospectively analysed. All cases met stringent eligibility criteria:

Inclusion criteria

1. Histologically confirmed primary carcinoma arising from a major or minor salivary gland.

2. Residual disease after curative-intent surgery, defined as either an unresectable positive margin owing to facial-nerve preservation or documented perineural invasion that precludes further resection.

3. No clinical or radiological evidence of regional nodal or distant metastasis at the time of surgery.

4. Seed implantation completed within 6–8 weeks after surgery.

5. Patients who were alive at last contact were required to have ≥5 years of follow-up. If a patient died within 5 years, follow-up ended at the date of death.

6. No additional external-beam radiotherapy or systemic chemotherapy to the head and neck was administered before or after ^{125}I seed implantation.

Exclusion criteria

1. Brachytherapy administered as the sole treatment without prior surgery.

2. Regional lymph-node or distant metastasis identified pre-operatively or intra-operatively.

3. Incomplete documentation of surgical margin status or invasive patterns.

4. Event-free survivors alive at last contact were excluded when follow-up was <5 years and no additional contact information existed.

Comprehensive baseline data (age, sex, tumour site, histological subtype) were collected. Post-implant follow-up involved scheduled clinical examinations and imaging. Overall survival (OS), measured from seed implantation to death or last contact, served as the primary endpoint, whereas local recurrence (LR) was designated as a secondary endpoint. This study was approved by the Institutional Review Board of Peking University Health Science Center (PUIRB; IRB00001052-13045), and conducted in accordance with the Declaration of Helsinki. Written informed consent was obtained from all participants.

External validation cohort

An independent, non-overlapping cohort of 74 consecutive patients who underwent surgery (with subsequent permanent ^{125}I seed implantation) between January and September 2020 at the same institution was assembled for external evaluation. Inclusion/exclusion criteria, endpoint definitions, image/dose processing, and follow-up procedures were identical to the derivation cohort. All survivors had accrued ≥5 years of follow-up. External-cohort analyses were performed under the same institutional ethics approval.

Study design

Prior to seed implantation, all patients underwent a pre-implant planning CT scan, which was used for delineation of the clinical target volume (CTV). All patients received low-dose-rate interstitial brachytherapy using permanent implantation of ^{125}I seeds (model 6711; Beijing Atom and High Technique Industries Inc, Beijing, China; (t_1/2, 59.6 days; energy level, 27.4–31.4 keV. Under image guidance, ^{125}I seeds were implanted into the clinical target volume (CTV) according to a preplanned distribution. The CTV encompassed the tumor bed and a 10-mm surrounding margin. Based on these images, a dedicated brachytherapy treatment planning system (BTPS; Beijing Astro Technology Ltd. Co., Beijing, China), was employed to design the dose distribution, aiming to ensure adequate coverage of the CTV with the prescribed dose while minimizing radiation exposure to surrounding normal tissues. The prescribed dose ranged from 80 to 120 Gy, delivered continuously over the radioactive decay period of the low-dose-rate (LDR) ^{125}I seeds. Within one week after implantation, all patients underwent a post-implant verification CT scan to confirm seed positions and evaluate the actual dose distribution. This verification CT clearly displayed the spatial distribution of the implanted seeds and was used by the treatment planning system to compute the three-dimensional dose distribution within the patient. The complete analytical workflow from data acquisition to model evaluation is illustrated in Figure 1.

For each patient, we exported both the pre-implant planning CT and the post-implant dose distribution as a voxelized 3D dose matrix mapped onto the CT for further analysis. In this study, we define “dosiomic” features as those derived from the 3D dose distribution within the target volume, and “radiomic” features as those derived from the CT image intensity distribution of the tumor.

Clinical variables

Clinical and treatment-related parameters were retrospectively collected from electronic medical records. These included patient age, sex, tumor size, pathological subtype, laterality (left vs. right), target volume (CTV), and the anatomical site of the primary lesion (parotid, submandibular or minor salivary gland). Treatment-specific variables encompassed the number of implanted seeds, the radioactivity of ^{125}I seeds , the number of implanted needles, and the prescribed radiation dose.

Dosimetric parameters

A total of nine dosimetric parameters were extracted from the dose–volume histograms (DVHs) for analysis and model development. The nine indices were D98, D95, D2, Dmean, Dmax, Dmin, homogeneity index (HI), external volume index (EI), and

conformity index (CI). D98, D95, and D2 represent the doses received by 98%, 95%, and 2% of the target volume, respectively, and are commonly used to assess minimum, near-prescription, and high-dose regions within the clinical target volume (CTV). Dmax and Dmin reflect the maximum and minimum point doses within the CTV, while Dmean indicates the average dose delivered to the target. HI quantifies dose uniformity within the target, with lower values indicating better homogeneity. CI evaluates how well the prescription dose conforms to the target volume, and EI estimates the proportion of irradiated tissue extending beyond the target.

Radiomic Features

All planning CT scans were resampled with B-spline interpolation to $2 \times 2 \times 2\,mm^3$ voxels to ensure geometric consistency. Feature extraction was performed with PyRadiomics 3.0, enabling every available image type—Original, Square, SquareRoot, Logarithm, Exponential, Gradient, two Laplacian-of-Gaussian volumes ($\sigma = 1$ and 3 mm) and the eight wavelet sub-bands—so that 16 derived images were analysed. Across these volumes we computed seven feature families: 14 shape descriptors (evaluated only on the Original image), 18 first-order statistics, and 75 texture variables obtained from GLCM (24), GLRLM (16), GLSZM (16), GLDM (14) and NGTDM (5), giving 1502 modelling features; a fixed bin width of 10 HU was applied for grey-level discretisation, and definitions follow IBSI conventions.

Dosiomic Feature

In contrast to conventional external-beam radiotherapy studies that interrogate the dose distribution calculated on the planning CT, the present work implemented a dedicated and stringent dosiomic workflow. The analysis began with a post-implant verification CT acquired after the placement of ^{125}I radioactive seeds. Each seed was individually localised on this scan, and a three-dimensional dose distribution was subsequently reconstructed from the recorded seed activity and coordinates using a TG-43-compliant brachytherapy treatment-planning system (BTPS; Beijing Astro Technology Ltd., Beijing, China).

The post-implant verification CT scan served as the primary imaging dataset for dose mapping. This volumetric CT, which acquired with contiguous axial slices was imported into the treatment planning workflow to visualize and identify all implanted ^{125}I seeds. Preprocessing of the CT included appropriate windowing and filtering to enhance the high-density seed artifacts against soft tissue background. Each seed appears as a small, elongated hyperdense object (approximately 4.5 mm length, 0.8 mm diameter often accompanied by streak artifacts. A trained observer manually localized the seed positions by scrolling through the CT slices and marking the centroid of each visible seed. Care was taken to cross-verify seed counts and coordinates in orthogonal views to ensure accurate 3D placement. This manual identification process established a set of seed coordinates in the CT image reference frame, effectively mapping the actual implant geometry for subsequent dose calculation. In cases of closely spaced seeds or imaging artifacts, the operator relied on slight adjustments of window/level and visual confirmation on multiple slices to distinguish individual seed locations. These identified seed coordinates on the CT constituted the ground truth post-implant source distribution for dosimetric analysis. The manually determined seed coordinates and their known activities were entered into the treatment-planning system. Its dose calculation engine follows the AAPM TG-43 formalism, the standard protocol for brachytherapy dosimetry in a water-equivalent medium[11].

All seeds were modeled as point sources with the specified ^{125}I model's emission characteristics. The planning system superimposed the dose contributions from each seed to obtain the cumulative dose distribution in the entire volume. The calculation produced a high-resolution 3D dose matrix spanning the region of interest. All dose calculations were performed to generate the total time-integrated dose. Following dose calculation, the verification CT was co-registered with the initial planning CT using rigid registration algorithms, ensuring accurate anatomical correspondence. The clinical target volume (CTV), originally delineated on the planning CT, was precisely propagated onto the verification CT to serve as the definitive region-of-interest for dosiomic analysis. The overall workflow for radiomic and dosiomic feature extraction—encompassing the planning CT with contoured CTV, the post-implant verification CT, and the reconstructed three-dimensional dose map—is illustrated in Figure 2.

Dose distributions within the defined CTV on the verification CT were then resampled via B-spline interpolation onto a uniform isotropic voxel grid of $2 \times 2 \times 2\,mm^3$, matching the spatial resolution and geometry of the radiomic analysis. Subsequently, discretization of the dose values was performed across the global minimum–maximum dose range using a fixed bin width of 1

Gy. These uniformly resampled and discretized three-dimensional dose matrices were subjected to feature extraction using PyRadiomics (version 3.0). Dosiomic feature extraction followed the identical PyRadiomics 3.0 pipeline described above, producing 1502 candidate features in total.

Model building

Prior to modelling, all numeric variables with > 20 % missingness were excluded, and the remaining gaps were filled using multivariate iterative imputation (MICE). Continuous predictors were z-score normalised and near-zero-variance features were discarded. Pairwise Spearman correlations were computed; when $|\rho| \geq 0.80$, the variable with the larger mean absolute correlation was removed. Endpoint-specific dimensionality reduction was performed using Least Absolute Shrinkage and Selection Operator (LASSO) regularization, tuned via an internal 5-fold cross-validation loop repeated 20 times. Features retained by LASSO were further inspected for multicollinearity, and those with a variance inflation factor (VIF) > 10 were eliminated. Using these final feature subsets, we fitted five multivariate models for each endpoint: clinical, DVH, radiomics, dosiomics, and hybrid. Cox proportional-hazards models were employed for all primary endpoints including overall survival (OS) and local recurrence (LR). To quantify the robustness of selected feature sets, the entire training cohort additionally underwent 20 × 5-fold stratified cross-validation, and the average Harrell's C-index across the resulting 100 validation folds was recorded.

Evaluation

Model performance was comprehensively evaluated using Cox proportional hazards regression for all primary endpoints, including overall survival (OS) and local recurrence (LR). For internal generalisation, models trained on the full training cohort were assessed on a held-out 30% validation cohort. The primary evaluation metric for all endpoints was Harrell's concordance index (C-index), reflecting the model's discriminative ability for time-to-event outcomes. Risk stratification was visualised using Kaplan–Meier survival curves, with survival distributions compared using log-rank tests. Ninety-five percent confidence intervals for performance metrics were obtained by bootstrapping the cohort's predicted risks without refitting the model.

Baseline clinical characteristics were compared between outcome groups using the Fisher exact test for categorical variables and the Mann–Whitney U test for continuous variables. All predictive models were fitted with Cox proportional-hazards regression; high-dimensional variable selection followed the workflow described in the Model building section. Model discrimination was quantified by Harrell's C-index on the held-out 30% validation cohort; 95% CIs were derived from bootstrap resamples of the validation-set predictions. Differences in C-index between models were evaluated using paired bootstrap resampling of the validation-set predictions; significance was inferred when the 95% CI of the paired difference excluded zero. Risk-stratification performance was visualised with Kaplan–Meier curves and compared using two-sided log-rank tests. All analyses were conducted in Python (version 3.8) and R software (version 3.6.3). A two-sided $P < 0.05$ was considered statistically significant.

Model performance was additionally assessed in an independent cohort of 74 patients operated between January and September 2020 (all survivors ≥5-year follow-up). This cohort was processed with the same feature set and preprocessing as the derivation pipeline. Performance was reported as Harrell's C-index (bootstrap 95% CI), time-dependent AUC at 1/3/5 years (IPCW), integrated Brier score, calibration-in-the-large and slope with decile-based calibration curves, decision-curve analysis (1/3/5 years), and Kaplan–Meier curves stratified by the median linear predictor with log-rank tests.

Results

Patients

A total of 263 patients were enrolled in this study, with the brachytherapy implantation procedures performed between April 2011 and December 2019. The median age at the time of treatment was 42 years (range, 17–79 years), and the median follow-up duration was 71 months (range, 11–165 months). During the follow-up period, locoregional failure occurred in 64 patients (24.3%), with a median time to failure of 33 months (range, 6–87 months). Baseline demographic and clinical characteristics of the study population are presented in Supplementary Table S1. In addition, an independent external cohort of 74 consecutive

patients operated between January and September 2020 at our institution (all survivors ≥ 5-year follow-up at data-lock) was analysed for external evaluation; 14 patients (18.9%) developed locoregional recurrence.

Feature Extraction and Robust Feature Selection

Using PyRadiomics, we initially extracted 1502 imaging-derived variables. Redundancy was addressed by calculating pairwise Spearman correlation coefficients for all radiomic features and eliminating, within each highly correlated pair ($|\rho| \geq 0.80$), the feature with the higher mean absolute correlation to the remainder of the set. This procedure reduced the radiomic feature pool to 207 non-redundant descriptors.

The same correlation-based filter was applied to the 1502 dosiomic variables, producing 332 robust features. All retained radiomic and dosiomic features were subsequently entered into model development.

Predictive Modeling for Local Recurrence: Univariate Cox Regression Analysis

Across individual features, 19 showed notable univariable associations (C-index > 0.60 and P < 0.05), thereby demonstrating significant discriminatory capacity. Among the clinical covariates, three routinely collected procedural parameters (Number of Seeds, Number of Needles, and Target Volume) each achieved a C-index above 0.60 and retained statistical significance, indicating that higher seed or needle counts and larger target volumes were significantly associated with an elevated recurrence risk. Among the DVH metrics, all investigated dose volume histogram parameters (Conformity Index [CI], D95, and Dmax) met the same criteria, underscoring the prognostic importance of high dose coverage (D95), hotspot control (Dmax), and geometric conformity (CI) for durable local control. In addition, seven intensity and texture based radiomic descriptors extracted from pre treatment CT images (original_GLSZM_ZonePercentage, original_FirstOrder_90Percentile, wavelet-LHL_FirstOrder_Minimum, wavelet-LHL_FirstOrder_Median, exponential_GLCM_Correlation, exponential_GLRLM_ShortRunEmphasis, and wavelet-LLH_GLSZM_SizeZoneNonUniformityNormalized) showed significant prognostic value, collectively capturing spatial heterogeneity across both low and high frequency image domains. Finally, six dosiomic features derived from the 3D dose distribution—four texture/first-order descriptors (wavelet-LLH_GLSZM_SizeZoneNonUniformity, original_GLRLM_RunLengthNonUniformity, wavelet-LHL_GLCM_ClusterTendency, and wavelet-LHL_FirstOrder_Maximum) and two dose-shape measures computed on the dose matrix (original_Shape_Maximum2DDiameterSlice and original_Shape_Sphericity)—showed significant associations with recurrence, suggesting that both intra-target dose heterogeneity and the geometry of the delivered dose contribute to LR risk.

Predictive Modeling for Local Recurrence: Multivariate Cox regression model

Using the preselected feature sets obtained from the overall selection pipeline, we fitted five block-wise multivariable Cox models (clinical, DVH, radiomics, dosiomics, hybrid) (Table 1). The clinical model, composed of three routine surgical variables, achieved a C-index of 0.79 in the training set and 0.73 (0.59–0.85) in the validation set, with an AIC of 423.09. The DVH model, incorporating CI, D95, and Dmax, reached training and validation C-indices of 0.70 and 0.69 (0.54–0.83), respectively, and an AIC of 434.08. The radiomics model, driven by seven high-ranking texture descriptors, posted a training C-index of 0.81 and an impressive validation C-index of 0.86 (0.78–0.92), accompanied by the lowest single-modality AIC of 408.23. The dosiomics model, built from six dose-texture and shape features, achieved a training C-index of 0.81; the validation C-index had the same point estimate (0.81; 95% CI 0.70–0.90) and an AIC of 410.17. To limit over-fitting, the hybrid model retained four cross-modal predictors—Target Volume, CI, wavelet-LLH_GLSZM_SizeZoneNonUniformity, and original_GLSZM_ZonePercentage—demonstrating that a larger target volume increased recurrence risk (P = .008), higher CI conferred a protective effect (P = .001), greater dose-texture heterogeneity elevated risk (P = .018), and original_GLSZM_ZonePercentage remained strongly prognostic (P < .001). This hybrid model achieved the highest overall performance, with training and validation C-indices of 0.87 (validation 0.78–0.94) and the lowest AIC of 402.90.

Table 1
Univariate and multivariate Cox proportional-hazards analysis

Feature		Univ. P	Univ. C-index	Multiv. P	Model C-index	AIC	Validation C-index (95% CI)
Clinical model					0.79	423.09	0.73 (0.59–0.85)
	Target Volume	< .001	0.67	0.074	–	–	–
	Number of Needles	< .001	0.72	0.440	–	–	–
	Number of Seeds	< .001	0.73	0.080	–	–	–
DVH model					0.70	434.08	0.69 (0.54–0.83)
	CI	< .001	0.64	0.001	–	–	–
	D95	< .001	0.62	0.002	–	–	–
	Dmax	0.007	0.61	0.902	–	–	–
Radiomics model					0.81	408.23	0.86 (0.78–0.92)
	original_GLSZM_ZonePercentage	< .001	0.73	0.097	–	–	–
	original_FirstOrder_90Percentile	0.001	0.68	0.149	–	–	–
	wavelet-LHL_FirstOrder_Minimum	< .001	0.68	0.065	–	–	–
	wavelet-LHL_FirstOrder_Median	< .001	0.69	0.001	–	–	–
	exponential_GLCM_Correlation	< .001	0.66	0.002	–	–	–
	exponential_GLRLM_ShortRunEmphasis	< .001	0.66	0.007	–	–	–
	wavelet-LLH_GLSZM_SizeZoneNonUniformityNormalized	< .001	0.62	0.018	–	–	–
Dosiomics model					0.81	410.17	0.81 (0.70–0.90)
	wavelet-LLH_GLSZM_SizeZoneNonUniformity	< .001	0.70	0.018	–	–	–
	original_GLRLM_RunLengthNonUniformity	0.031	0.72	0.034	–	–	–
	original_Shape_Maximum2DDiameterSlice	< .001	0.74	0.027	–	–	–
	original_Shape_Sphericity	< .001	0.71	0.011	–	–	–
	wavelet-LHL_GLCM_ClusterTendency	0.008	0.60	0.016	–	–	–
	wavelet-LHL_FirstOrder_Maximum	0.005	0.63	0.009	–	–	–
Hybrid model					0.87	402.90	0.87 (0.78–0.94)
	Target Volume	–	–	–	–	–	–
	wavelet-LLH_GLSZM_SizeZoneNonUniformity	–	–	–	–	–	–
	original_GLSZM_ZonePercentage	–	–	–	–	–	–

Feature	Univ. P	Univ. C-index	Multiv. P	Model C-index	AIC	Validation C-index (95% CI)
CI	–	–	–	–	–	–

Univ. = univariate Cox regression; Multiv. = multivariate Cox regression.

Predictive Modeling for Local Recurrence: Kaplan–Meier estimates

To capture the joint prognostic effect of the four hybrid predictors, we calculated an individual risk score (linear predictor) from the hybrid Cox model and dichotomised patients at the median value. Kaplan–Meier curves generated from this composite score showed a clear separation between low- and high-risk groups across all datasets (Fig. 3A). In the whole cohort the difference was highly significant (log-rank $P < .001$); the same pattern appeared in the training set ($P = .002$) and remained evident in the validation set ($P = 2.3 \times 10^{-5}$).

Predictive Modeling for Local Recurrence: Discriminative Performance of Multimodal Prediction Models

To further evaluate the discrimination performance of each model, receiver operating characteristic (ROC) curves were constructed using validation set (Fig. 4A). The hybrid model yielded the highest area under the curve (AUC = 0.93), followed by the radiomics (AUC = 0.90), dosiomics (AUC = 0.89), clinical (AUC = 0.80), and DVH (AUC = 0.73) models. These results indicate that the integration of multi-modal features substantially improved predictive accuracy compared to single-modality models.

External validation for Local Recurrence

In the independent cohort, the hybrid Cox model showed consistent out-of-sample performance (Harrell's C-index = 0.714). IPCW time-dependent AUCs at 1/3/5 years were 0.645/0.722/0.732, respectively, and the overall prediction error was low (IBS = 0.090). Decision-curve analysis indicated positive net benefit across clinically relevant thresholds (~ 0.10–0.40). Kaplan–Meier curves stratified by the median linear predictor were clearly separated. Figure 5 summarises the 60-month ROC (A), calibration (B), DCA (C), and KM (D) results.

Predictive Modeling for survival: Univariate Cox Regression Analysis

Univariable Cox regression was performed for all candidate covariates in the training cohort, and discriminative ability was quantified by the Harrell concordance index (C-index). Among the dosiomic metrics, original_glrlm_RunLengthNonUniformity exhibited the greatest prognostic discrimination (C-index = 0.65, $P < 0.001$). Within the radiomic domain, exponential_glszm_ZoneVariance yielded the highest performance (C-index = 0.61, $P = 0.013$). No clinical variable achieved a C-index > 0.60; the two best-performing clinical factors were target volume (C-index = 0.58, $P = 0.023$) and age (C-index = 0.52). For DVH parameters, only Dmax exceeded a C-index of 0.50, registering a value of 0.59.

Based on their C-index ranking, the top two variables from each category (with DVH restricted to Dmax alone) were retained for subsequent multivariable modelling, thereby providing the foundation for the integrative prognostic model.

Predictive Modeling for survival: Multivariate Cox Regression Analysis

Multivariate Cox analysis showed that the clinical, DVH, radiomics, dosiomics, and hybrid models provided markedly different prognostic yields (Table 2). The clinical model, based on target volume and age, offered limited discrimination (training C-index 0.59, validation 0.54, 95% CI 0.45–0.64; AIC 1254.25) and no independent covariate retained significance. The DVH model achieved a training C-index of 0.62 and a validation C-index of 0.57 (0.47–0.66) with an AIC of 1256.94; however, Dmax did not reach multivariate significance ($P = 0.470$), suggesting that maximum-dose hotspots alone provide modest survival discrimination. The radiomics pair exponential_glszm_ZoneVariance and exponential_glcm_Correlation reached a validation C-index of 0.60 (AIC 1254.44). By contrast, the dosiomics model—driven by original_glrlm_RunLengthNonUniformity and log-sigma-3-mm-3D_glszm_SmallAreaEmphasis—yielded the best single-block performance (training C-index 0.65, validation 0.60, 0.51–0.70; AIC 1242.39), with RunLengthNonUniformity remaining strongly predictive ($P < 0.001$). In the internally held-out validation subset, the parsimonious hybrid model—which combined target volume, Dmax, exponential_glszm_ZoneVariance and

original_glrlm_RunLengthNonUniformity—achieved the highest discrimination (C-index 0.63, 95% CI 0.53–0.72; AIC 1241.24), marginally exceeding the dosiomics model.

Table 2
Univariate and multivariate Cox proportional-hazards analysis

Feature		Univ. P	Univ. C-index	Multiv. P	Model C-index	AIC	Validation C-index (95% CI)
Clinical model					0.59	1254.25	0.54(0.45–0.64)
	Target volume	0.023	0.58	0.622	–	–	–
	age	0.680	0.52	0.380	–	–	–
DVH model					0.62	1256.94	0.57(0.47–0.66)
	Dmax	0.712	0.59	0.470	–	–	–
Radiomics model					0.59	1254.44	0.60 (0.50–0.68)
	exponential_glszm_ZoneVariance	0.013	0.61	0.255	–	–	–
	exponential_glcm_Correlation	0.077	0.55	0.695	–	–	–
Dosiomics model					0.65	1242.39	0.60(0.51–0.70)
	original_glrlm_RunLengthNonUniformity	< .001	0.65	< .001	–	–	–
	log-sigma-3-mm-3D_glszm_SmallAreaEmphasis	0.393	0.56	0.381	–	–	–
Hybrid model					0.65	1241.24	0.63 (0.53–0.72)
	Target volume	–	–	–	–	–	–
	Dmax	–	–	–	–	–	–
	exponential_glszm_ZoneVariance	–	–	–	–	–	–
	original_glrlm_RunLengthNonUniformity	–	–	–	–	–	–

Predictive Modeling for survival: Kaplan–Meier Survival Estimates

Using the risk score derived from the hybrid Cox model, patients were dichotomised at the cohort-specific median and Kaplan–Meier curves were plotted for the entire cohort, the training subset, and the held-out validation subset (Fig. 3B). Pronounced risk separation was observed in the full dataset: high-risk patients showed a markedly lower long-term survival than their low-risk counterparts, with the curves diverging early and the difference reaching strong statistical significance (log-rank $P = 1.4 \times 10^{-5}$). An almost identical pattern was reproduced in the training cohort (log-rank $P = 1.3 \times 10^{-6}$). Although the same directional trend persisted in the independent validation set, the log-rank test did not reach significance ($P = 0.47$), a finding that is compatible with the limited number of death events in this smaller subset. Collectively, these data confirm that the composite hybrid score stratifies patients into distinct survival strata in the development cohort and maintains prognostic directionality after internal validation.

Predictive Modeling for survival: Discriminative Performance of Multimodal Prediction Models

Receiver operating characteristic (ROC) analysis on the validation cohort (Fig. 4B) showed that the hybrid model provided the highest discriminative accuracy for overall survival (AUC = 0.75), outperforming the dosiomics (AUC = 0.70), clinical (AUC = 0.65), and radiomics (AUC = 0.65) models, while the DVH model displayed only poor discrimination (AUC = 0.48). The incremental gain from 0.70 to 0.75 underscores the added value of combining complementary clinical, geometric-dose, image-texture, and dose-texture information; conversely, the negligible difference between the clinical and radiomics blocks and the weak DVH performance indicate that single-domain features alone are insufficient for reliable risk prediction in this cohort. Overall, these ROC results corroborate the Kaplan–Meier findings and highlight the hybrid model as the most powerful tool for individualised survival prognostication.

External validation for overall survival

In the independent cohort, the hybrid Cox model demonstrated good out-of-sample performance. Harrell's C-index was 0.859. IPCW time-dependent AUCs at 1/3/5 years were 0.945 / 0.887 / 0.909, respectively. The overall prediction error was low (IBS = 0.030). Decision-curve analysis indicated positive net benefit over "treat-all/none" across clinically relevant thresholds (~ 0.10–0.40). Kaplan–Meier curves stratified by the median linear predictor remained clearly separated, consistent with the discrimination metrics. Figure 6 summarises the 60-month ROC (A), calibration (B), DCA (C), and KM (D) results.

Discussion

In this study, we developed and compared five prognostic models—clinical, dose-volume histogram (DVH), radiomic, dosiomic, and an integrated hybrid model—to predict local recurrence (LR) and overall survival (OS) in salivary gland cancer patients treated with low-dose-rate brachytherapy. Our findings demonstrate that the integrated hybrid model, combining clinical, DVH, radiomic, and dosiomic features, achieved the highest predictive accuracy for LR (internal validation C-index 0.87; 95% CI 0.78–0.94), surpassing each single-modality approach. This result emphasizes the complementary value of multi-modal feature fusion for predicting locoregional control, where tumor phenotype, procedural parameters, and dose heterogeneity collectively contribute to recurrence risk. In a temporally independent external cohort, the structure-fixed hybrid model maintained moderate out-of-sample performance (Harrell's C-index 0.714; time-dependent AUCs at 1/3/5 years 0.645/0.722/0.732; IBS 0.090), with positive net benefit on DCA and clear KM separation (Fig. 5).

When considering single-modality models for LR prediction, radiomics provided the strongest discrimination (internal validation C-index 0.86, 95% CI 0.78–0.92; AUC 0.90), substantially outperforming the clinical model by 13 percentage points (C-index 0.73, 95% CI 0.59–0.85; AUC 0.80) and the DVH model by 17 points (C-index 0.69, 95% CI 0.54–0.83; AUC 0.73). The most influential radiomic features included heterogeneity metrics (e.g., original_GLSZM_ZonePercentage) and intensity-based descriptors (e.g., wavelet-LHL_FirstOrder_Median), which likely reflect underlying aggressive biological characteristics such as necrosis, hypoxia, or clonal diversity, and thus serve as reliable imaging biomarkers for recurrence risk stratification[12].

For OS prediction, the parsimonious hybrid model (Target Volume, Dmax, exponential_glszm_ZoneVariance, original_glrlm_RunLengthNonUniformity) achieved the highest discrimination (internal validation C-index 0.63, 95% CI 0.53–0.72; AIC 1241.24), marginally exceeding the best single-modality dosiomics model (training C-index 0.65; internal validation 0.60, 95% CI 0.51–0.70; AIC 1242.39). RunLengthNonUniformity (dose texture) and ZoneVariance (CT texture) remained independently prognostic. This pattern indicates that while feature fusion confers a clear benefit for LR, its gain for OS is modest rather than dominant; nonetheless, dosiomic descriptors still contribute unique dose–heterogeneity information that is not captured by clinical or radiomic variables alone. Several factors may explain the modest incremental benefit for OS: First, OS is influenced by systemic progression and comorbidities that our dataset only partially captures; Second, adding variables with small effect sizes or multicollinearity can dilute the prognostic signal of key dose-texture descriptors[13]; Third, limited event numbers constrain model complexity and penalise additional predictors in penalised Cox regression. In summary, fusing clinical, radiomic and dosiomic data offers the greatest advantage for LR prediction, but for OS the same fusion may dilute or mask prognostic information. Importantly, in the external cohort the same four-feature hybrid specification preserved strong discrimination for OS (Harrell's C-index 0.859; AUCs at 1/3/5 years 0.945/0.887/0.909; IBS 0.030), with positive DCA and clear KM separation (Fig. 6).

Our study is among the first to apply radiomics and dosiomics modeling to salivary gland tumors treated with brachytherapy, and the results both reinforce and extend findings from prior research in related domains. Radiomics has been extensively studied in head and neck cancers (mostly in external beam radiotherapy settings), showing promise in prognostication. Many studies have reported that CT or MRI- based radiomic signatures can stratify patients by risk of recurrence or death, owing to radiomics' ability to quantify intratumoral heterogeneity invisible to the human eye.[14–16] Recent radiotherapy studies in head-and-neck cancer have consistently demonstrated the prognostic value of radiomics models. Bogowicz et al. combined CT-based radiomic features from the primary tumour (PT) and metastatic lymph nodes (LN), achieving a C-index of 0.67 for loco-regional control in an external cohort—an improvement of about 0.04 over a PT-only model (0.63)[17]. Liu et al. used a pre-treatment ^{18}F-FDG PET/CT radiomics score plus clinical variables to construct a nomogram that yielded a validation C-index of 0.77 (95% CI 0.70–0.84) for overall survival, nearly 0.09 higher than their traditional clinical model (~ 0.68)[18]. In our salivary-gland LDR-brachytherapy cohort, a CT-radiomics model increased the local-recurrence C-index from 0.73 (clinical only) to 0.86, a gain of 0.13. This improvement is broadly similar to the 0.04–0.10 range reported in the above studies, further underscoring the capacity of radiomics to capture intratumour heterogeneity and enhance prognostic discrimination. Moreover, our temporal external validation corroborates the transportability of the hybrid specification for both LR and OS.

Dosiomics has long been applied to predict radiation-induced toxicities, and recent work now shows clear value for tumour-control end points as well. Liu et al. analysed an IMRT cohort of advanced hypopharyngeal cancer and built an integrated model that combined radiomic, dosiomic and clinical variables; in external validation the loco-regional-control C-index reached 0.815. This demonstrates that spatial dose features add independent predictive signal for recurrence[19]. Nakano et al. studied ^{125}I low-dose-rate prostate brachytherapy and, using only a handful of dosiomic texture and shape descriptors, raised the AUC for predicting biochemical relapse to 0.86, well above traditional DVH metrics such as D90 or V100[20]. Consistent with these findings, our salivary-gland LDR-brachytherapy study achieved a dosiomics C-index of 0.81 for local-recurrence prediction. Collectively, these results underscore the critical role of detailed dose-distribution analysis in enhancing treatment-outcome modelling. Compared with previous head-and-neck tumor local-control models, our hybrid model yields an AUC of 0.93 for recurrence, on par with other single-center deep-learning or PET/CT fusion studies (AUC 0.93–0.96)[21, 22]. The high score mainly reflects the dataset's homogeneity, a clear event definition, and complementary imaging-dose signals. A 95% confidence interval of 0.78–0.94 was obtained by bootstrapping the validation-set predictions while holding the model fixed. After adding temporal external validation (Figs. 5 and 6), future work will prioritise coefficient-locked, multi-centre validation and pre-specified calibration updating.

Despite this progress, no previous study has applied radiomic or dosiomic modelling specifically to salivary-gland malignancies treated with brachytherapy, which are relatively rare. Salivary-gland cancers possess unique histologies and present clinical challenges such as perineural spread and a high risk of local recurrence. This paucity of radiomic and dosiomic investigations represents a significant knowledge gap, which the present study aims to fill. We demonstrate that even in a small, single-institution cohort, multi-modal AI models combining imaging and dose information can predict outcomes and behave consistently with radiomics theory and findings from more common cancers. This proof-of-concept shows that radiomics and dosiomics can be successfully extended to salivary-gland brachytherapy, offering novel insights for understudied tumour sites and broadening the scope of personalised radiotherapy research.

Several limitations warrant discussion. First, because salivary-gland carcinoma treated with low-dose-rate brachytherapy is uncommon, our cohort was relatively small and drawn from a single institution. This restricted sample size reduces statistical power, limits generalisability, and heightens the risk of over-fitting. Second, seed-related streak/blooming artefacts could bias texture quantification despite preprocessing, and the study focused exclusively on CT-based radiomics without incorporating additional modalities or molecular data, which might further enhance prediction. Going forward, multi-centre, coefficient-locked validation with formal calibration updating will be necessary to confirm clinical deployability.

Conclusion

This study demonstrates that CT-based radiomics and post-implant dosiomics carry significant prognostic value for patients with salivary-gland carcinoma treated with ^{125}I low-dose-rate brachytherapy. These findings close an important knowledge gap in

SGC brachytherapy outcome modelling and suggest that detailed image- and dose-based biomarkers can refine risk stratification beyond traditional DVH metrics. Future work should pursue coefficient-locked, multi-centre validation with pre-specified recalibration, and evaluate workflow-level impact on risk-adapted follow-up and adjuvant decision-making.

Declarations

Ethics approval and consent to participate

This study was approved by the Institutional Review Board of Peking University Health Science Center (PUIRB; IRB00001052-13045), and conducted in accordance with the Declaration of Helsinki. Written informed consent was obtained from all participants.

Consent for publication

Not applicable (no individual, identifiable data are included in this article).

Clinical trial registration

Clinical trial number: not applicable. (Observational retrospective study; no prospective trial registration.)

Funding

This work was supported by the Beijing Natural Science Foundation (No. Z240003). The funders had no role in study design, data collection/analysis, decision to publish, or manuscript preparation.

Data availability

The datasets generated and/or analysed during the current study contain patient information and are not publicly available due to institutional and legal restrictions. De-identified derived data (radiomics/dosiomics/DVH feature matrices and train/validation split indices) together with the analysis code are available from the corresponding authors upon reasonable request and subject to a data-use agreement and ethics approval.

Competing interests

The authors declare no competing interests.

Authors' contributions

ZL and GZ conceived and designed the study, performed the statistical modelling, and drafted the manuscript. XW collected and curated the clinical and imaging data. ZX implemented radiomics/dosiomics feature extraction and data preprocessing. ZL, GZ, and ZX prepared the figures. YZ verified clinical data, contributed to interpretation, and critically revised the manuscript. BL and MH supervised the project and served as corresponding authors. ZL and GZ contributed equally to this work. All authors reviewed and approved the final manuscript.

References

1. Geiger, Jessica L et al. "Management of Salivary Gland Malignancy: ASCO Guideline." Journal of clinical oncology : official journal of the American Society of Clinical Oncology vol. 39,17 (2021): 1909-1941. doi:10.1200/JCO.21.00449
2. Liu, Shu-Ming et al. "The efficacy of iodine-125 permanent brachytherapy versus intensity-modulated radiation for inoperable salivary gland malignancies: study protocol of a randomised controlled trial." BMC cancer vol. 16 193. 7 Mar. 2016, doi:10.1186/s12885-016-2248-7
3. Zhong, Yiwei et al. "Sole brachytherapy for inoperable, recurrent, and irradiated salivary gland cancer." Radiotherapy and oncology : journal of the European Society for Therapeutic Radiology and Oncology vol. 190 (2024): 110022. doi:10.1016/j.radonc.2023.110022

4. Jiang, Wen-Mei et al. “A Parsimonious Prognostic Model and Heat Map for Predicting Survival Following Adjuvant Radiotherapy in Parotid Gland Carcinoma With Lymph Node Metastasis.” Technology in cancer research & treatment vol. 20 (2021): 15330338211035257. doi:10.1177/15330338211035257
5. Lambin, Philippe et al. “Radiomics: extracting more information from medical images using advanced feature analysis.” European journal of cancer (Oxford, England : 1990) vol. 48,4 (2012): 441-6. doi:10.1016/j.ejca.2011.11.036
6. Yolchuyeva, Sevinj et al. “A Radiomics-Clinical Model Predicts Overall Survival of Non-Small Cell Lung Cancer Patients Treated with Immunotherapy: A Multicenter Study.” Cancers vol. 15,15 3829. 28 Jul. 2023, doi:10.3390/cancers15153829
7. Cheng, Nai-Ming et al. “Development and validation of a prognostic model incorporating [18F]FDG PET/CT radiomics for patients with minor salivary gland carcinoma.” EJNMMI research vol. 10,1 74. 6 Jul. 2020, doi:10.1186/s13550-020-00631-3
8. Sun, Lingyue et al. “Do Dosiomic Features Extracted From Planned 3Dimensional Dose Distribution Improve Biochemical Failure-Free Survival Prediction: an Analysis Based on a Large Multi-Institutional Data Set.” Advances in radiation oncology vol. 8,5 101227. 27 Mar. 2023, doi:10.1016/j.adro.2023.101227
9. Murakami Y, Soyano T, Kozuka T, et al. Dose-Based Radiomic Analysis (Dosiomics) for Intensity Modulated Radiation Therapy in Patients With Prostate Cancer: Correlation Between Planned Dose Distribution and Biochemical Failure. Int J Radiat Oncol Biol Phys. 2022;112(1):247-259. doi:10.1016/j.ijrobp.2021.07.1714
10. Zhang, Zhen et al. “Radiomics and Dosiomics Signature From Whole Lung Predicts Radiation Pneumonitis: A Model Development Study With Prospective External Validation and Decision-curve Analysis.” International journal of radiation oncology, biology, physics vol. 115,3 (2023): 746-758. doi:10.1016/j.ijrobp.2022.08.047
11. Williamson JF, Butler W, Dewerd LA, et al. Recommendations of the American Association of Physicists in Medicine regarding the impact of implementing the 2004 task group 43 report on dose specification for 103Pd and 125I interstitial brachytherapy. Med Phys. 2005;32(5):1424-1439. doi:10.1118/1.1884925
12. Aerts HJ, Velazquez ER, Leijenaar RT, et al. Decoding tumour phenotype by noninvasive imaging using a quantitative radiomics approach [published correction appears in Nat Commun. 2014;5:4644. Cavalho, Sara [corrected to Carvalho, Sara]]. Nat Commun. 2014;5:4006. Published 2014 Jun 3. doi:10.1038/ncomms5006
13. Ruud Kjær EK, Jensen JS, Jakobsen KK, et al. The Impact of Comorbidity on Survival in Patients With Head and Neck Squamous Cell Carcinoma: A Nationwide Case-Control Study Spanning 35 Years. Front Oncol. 2021;10:617184. Published 2021 Feb 17. doi:10.3389/fonc.2020.617184
14. Xu H, Abdallah N, Marion JM, et al. Radiomics prognostic analysis of PET/CT images in a multicenter head and neck cancer cohort: investigating ComBat strategies, sub-volume characterization, and automatic segmentation. Eur J Nucl Med Mol Imaging. 2023;50(6):1720-1734. doi:10.1007/s00259-023-06118-2
15. Wang TW, Wang CK, Hong JS, et al. Prognostic power of radiomics in head and neck cancers: Insights from a meta-analysis. Comput Methods Programs Biomed. 2025;262:108683. doi:10.1016/j.cmpb.2025.108683
16. Tortora M, Gemini L, Scaravilli A, et al. Radiomics Applications in Head and Neck Tumor Imaging: A Narrative Review. Cancers (Basel). 2023;15(4):1174. Published 2023 Feb 12. doi:10.3390/cancers15041174
17. Bogowicz M, Tanadini-Lang S, Guckenberger M, Riesterer O. Combined CT radiomics of primary tumor and metastatic lymph nodes improves prediction of loco-regional control in head and neck cancer. Sci Rep. 2019;9(1):15198. Published 2019 Oct 23. doi:10.1038/s41598-019-51599-7
18. Liu Z, Cao Y, Diao W, Cheng Y, Jia Z, Peng X. Radiomics-based prediction of survival in patients with head and neck squamous cell carcinoma based on pre- and post-treatment 18F-PET/CT. Aging (Albany NY). 2020 Jul 16;12(14):14593-14619. doi: 10.18632/aging.103508. Epub 2020 Jul 16. PMID: 32674074; PMCID: PMC7425452.
19. Liu H, Zhao D, Huang Y, et al. Comprehensive prognostic modeling of locoregional recurrence after radiotherapy for patients with locoregionally advanced hypopharyngeal squamous cell carcinoma. Front Oncol. 2023;13:1129918. Published 2023 Mar 21. doi:10.3389/fonc.2023.1129918
20. Nakano M, Kaji S, Kawakami S, Tsumura H, Imae T, Tanaka Y, Fujii K, Kainuma T, Yamazaki R, Uchida A, Kaneko H, Fujino M, Hata C, Murakami Y, Hashimoto M, Ishiyama H. Dosiomic predictors of biochemical failure in patients with localized prostate cancer treated with Iodine-125 low-dose-rate brachytherapy. Radiat Oncol. 2025 Apr 16;20(1):56. doi: 10.1186/s13014-025-02619-6

21. Zhang Q, Wang K, Zhou Z, Qin G, Wang L, Li P, Sher D, Jiang S, Wang J. Predicting local persistence/recurrence after radiation therapy for head and neck cancer from PET/CT using a multi-objective, multi-classifier radiomics model. Front Oncol. 2022 Sep 29;12:955712. doi: 10.3389/fonc.2022.955712. PMID: 36248979; PMCID: PMC9557184.
22. Fh T, Cyw C, Eyw C. Radiomics AI prediction for head and neck squamous cell carcinoma (HNSCC) prognosis and recurrence with target volume approach. BJR Open. 2021 Jul 5;3(1):20200073. doi: 10.1259/bjro.20200073

Figures

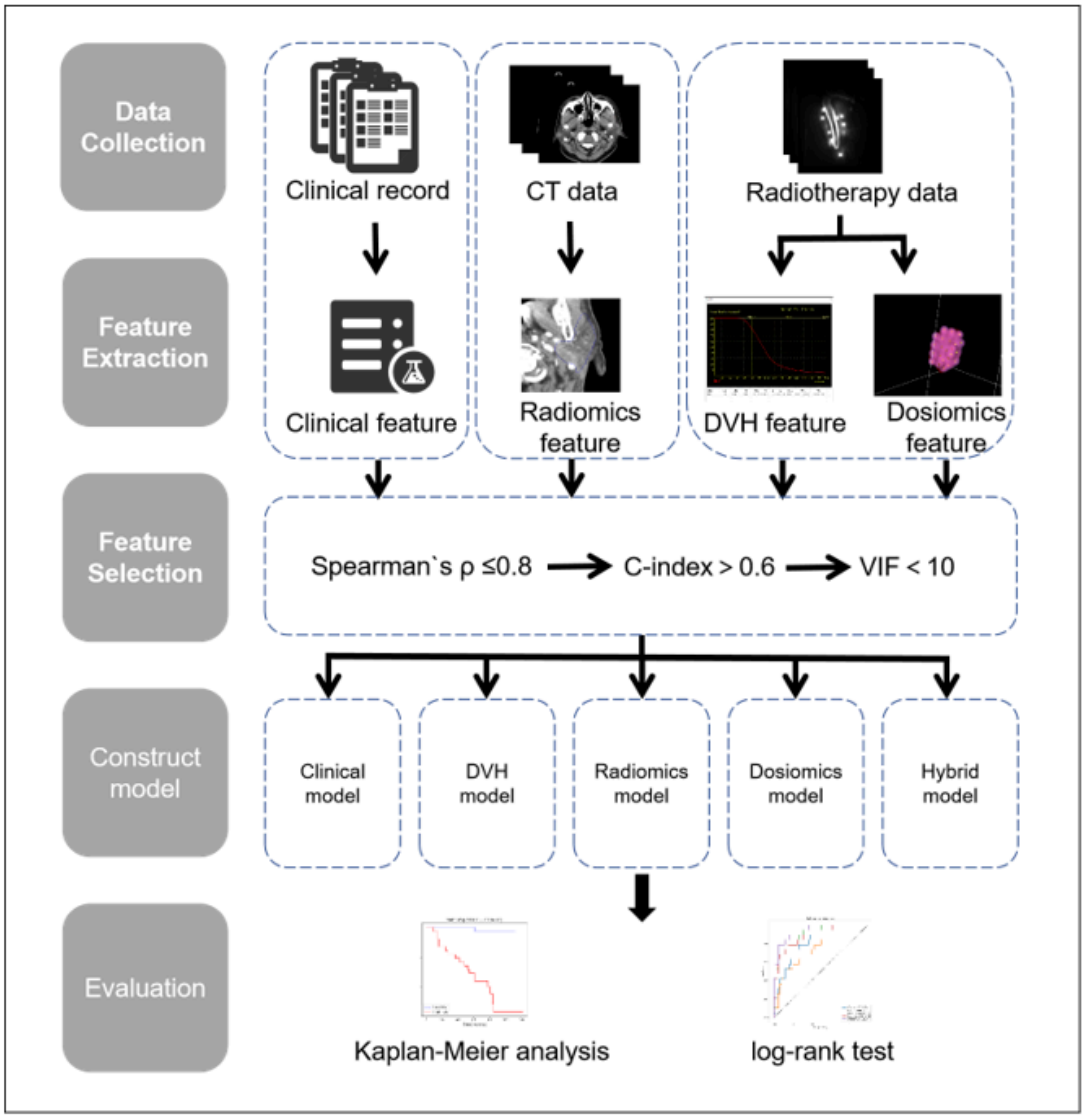


Figure 1

Study workflow. Overall workflow of the study. Abbreviations: CT = computed tomography; DVH = dose-volume histogram; VIF = variance inflation factor.

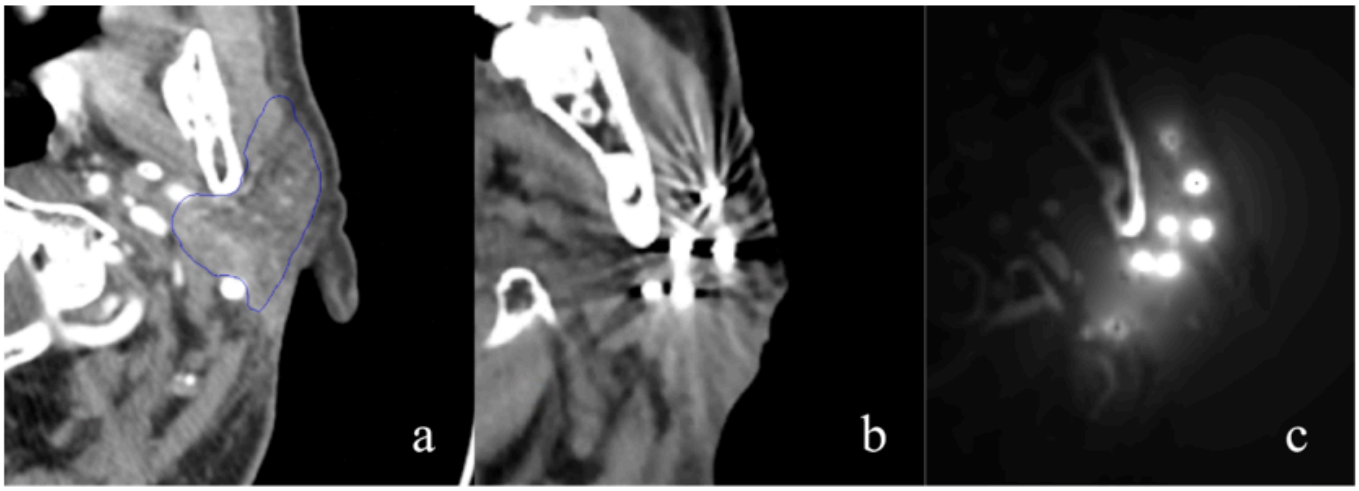


Figure 2

Representative planning, verification, and dose-distribution volumes used for radiomic and dosiomic analysis.
(a) Contrast-enhanced planning CT with the clinical target volume (CTV) manually contoured (blue line); radiomic features were extracted from this image set.
(b) Post-implant verification CT acquired after 125I seed placement, illustrating the high-density seeds and associated metallic artefacts; this scan served as the geometric basis for dose reconstruction.
(c) Calculated three-dimensional dose map (grayscale render) confined to the same axial slice, and dosiomic features were derived from this voxelised dose distribution.

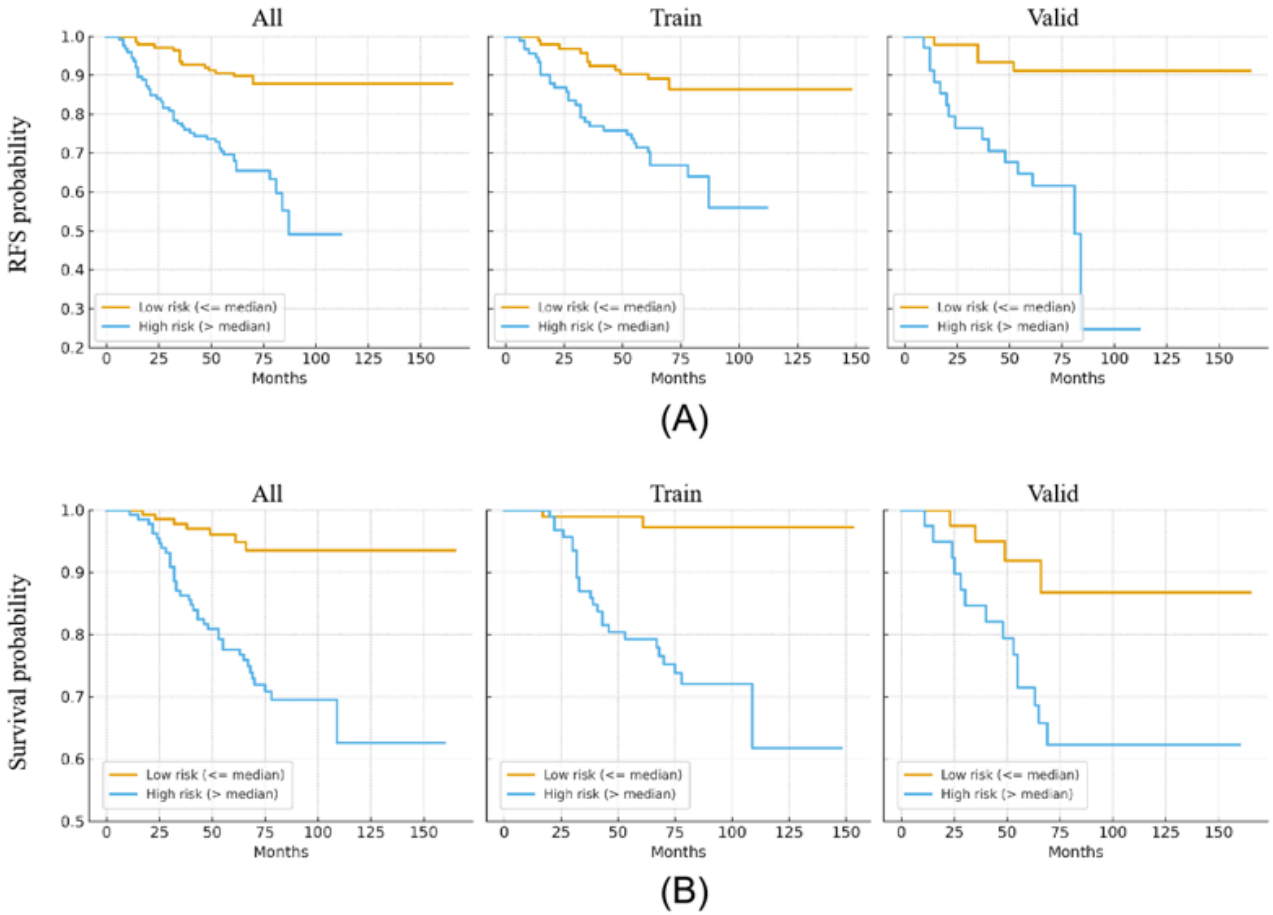


Figure 3

(A) Kaplan–Meier curves for local-recurrence-free survival stratified by the median hybrid score in the whole, training, and validation cohorts. (B) Kaplan–Meier curves for overall survival stratified by the median hybrid risk score (blue = low risk; red = high risk).

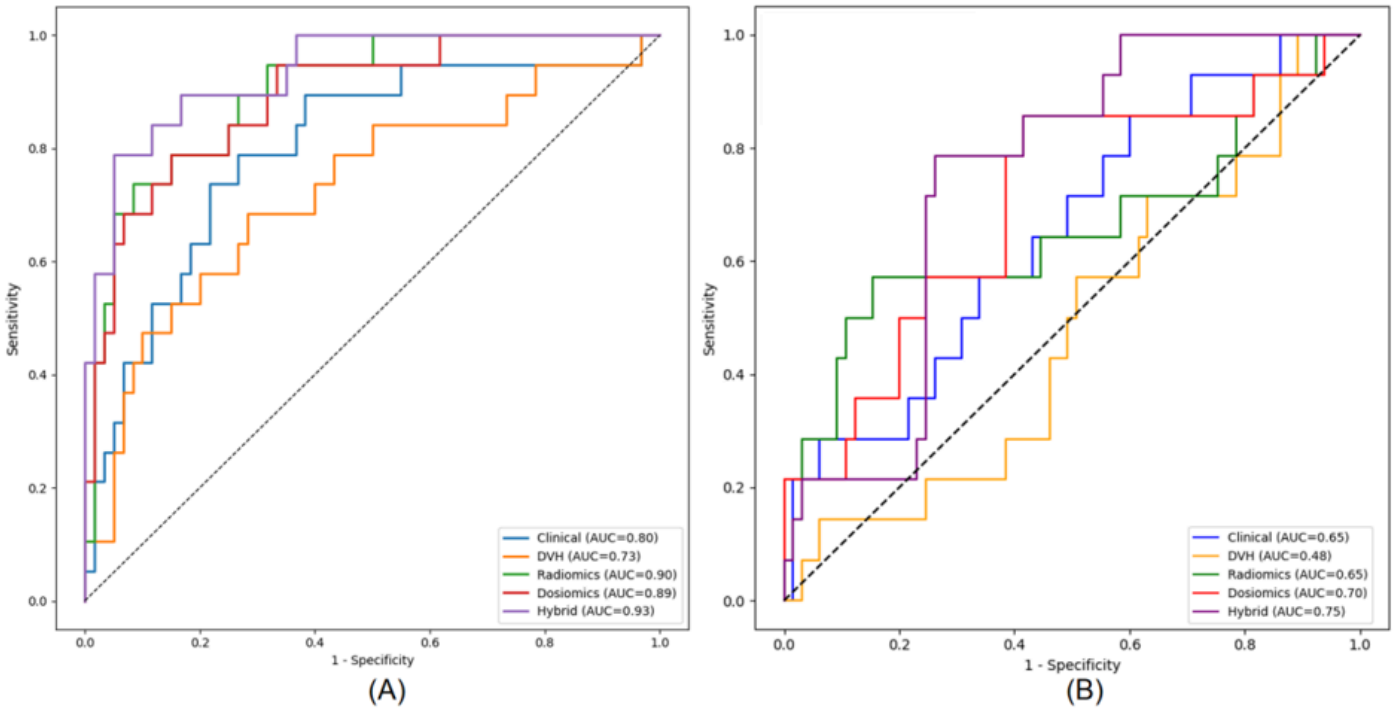


Figure 4

(A) ROC curves for internal validation of local-recurrence prediction models: clinical (blue), DVH (orange), radiomics (green), dosiomics (red), and hybrid (purple); the hybrid model achieved the highest AUC (0.93). (B) ROC curves for internal validation of overall-survival prediction models with the same color scheme; the hybrid model yielded the highest AUC (0.75).

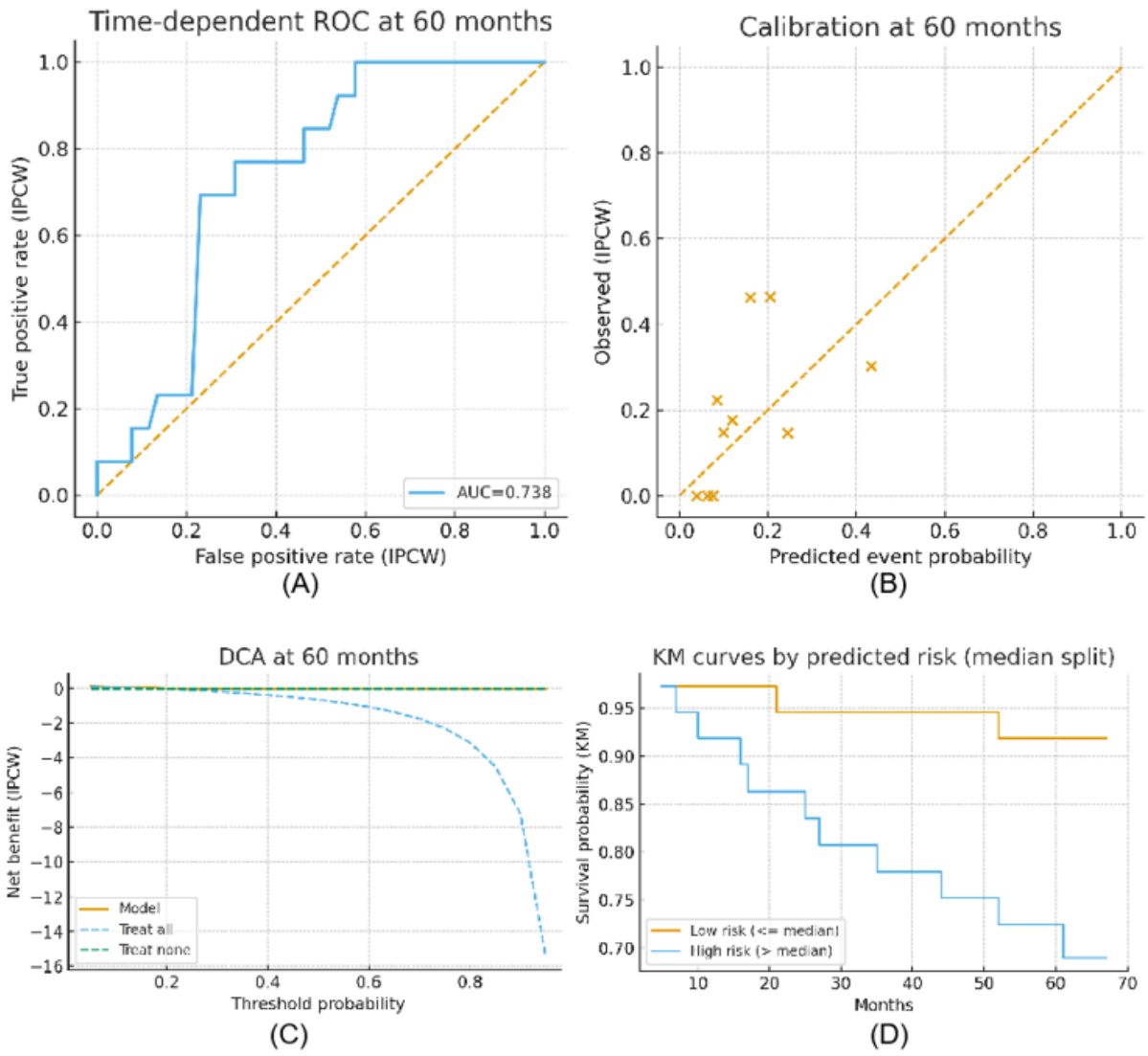


Figure 5

External validation of the hybrid model for local recurrence at 60 months.
(A) Time-dependent ROC with IPCW; the area under the curve (AUC) is shown in the panel.
(B) Calibration plot at 60 months: predicted event probability versus observed IPCW probability; the dashed 45° line indicates perfect calibration.
(C) Decision-curve analysis (DCA) at 60 months comparing the model with “treat-all” and “treat-none” strategies; net benefit is plotted across threshold probabilities.
(D) Kaplan–Meier curves of local-recurrence-free survival stratified by the median predicted risk (low vs high).

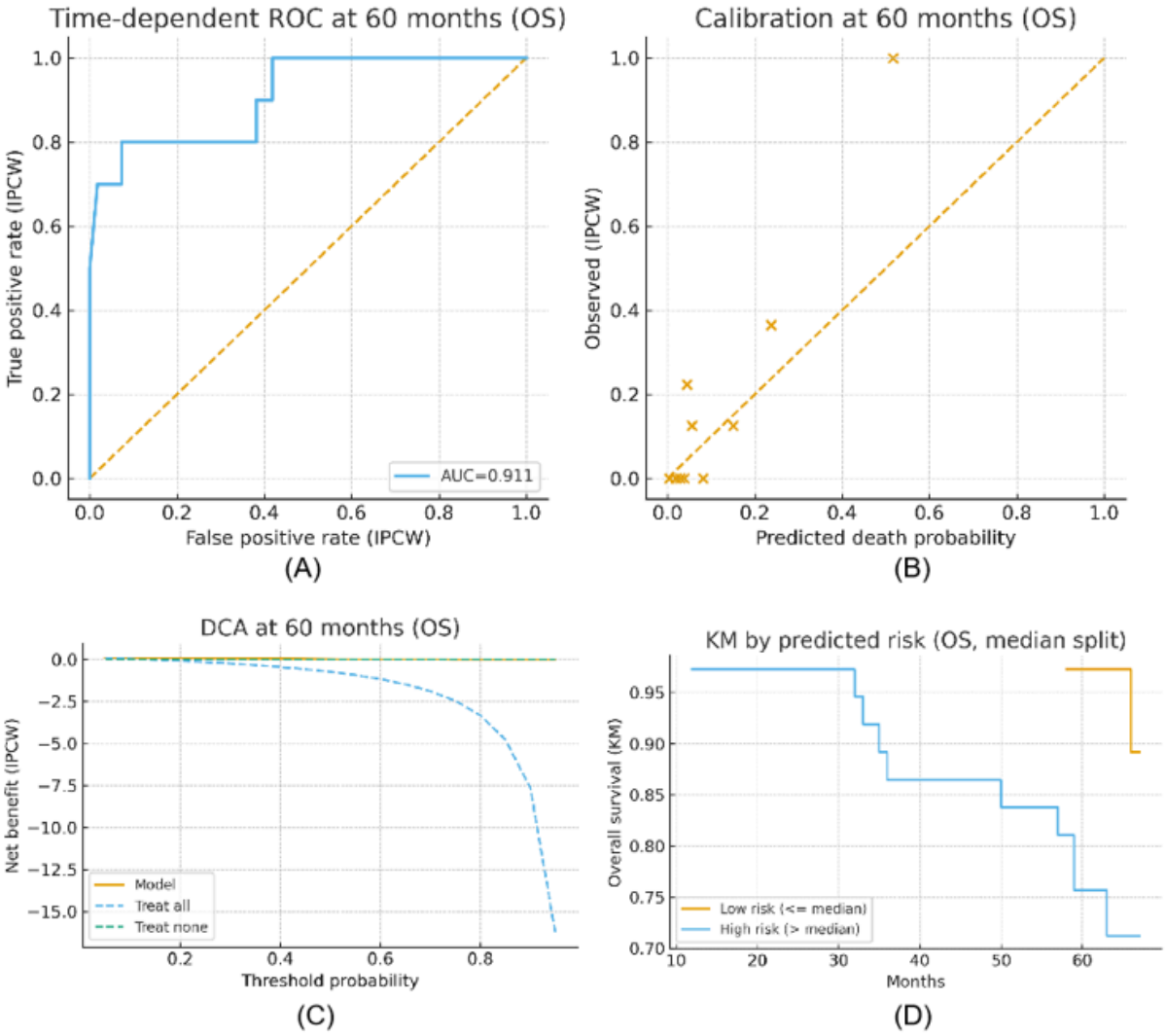


Figure 6

External validation of the hybrid model for overall survival at 60 months.
(A) Time-dependent ROC with IPCW; panel shows AUC at 60 months.
(B) Calibration plot at 60 months: predicted death probability vs observed IPCW probability; the dashed 45° line indicates perfect calibration.
(C) Decision-curve analysis (DCA) at 60 months comparing the model with “treat-all” and “treat-none” strategies.
(D) Kaplan–Meier curves of overall survival stratified by the median predicted risk.

Supplementary Files

This is a list of supplementary files associated with this preprint. Click to download.

- SupplementaryTable.docx